

Observation of topology of non-Hermitian systems without chiral symmetry

Shuo Wang(王硕), Zhengjie Kang(康正杰), Hao Li(李浩), Jiaojiao Li(李姣姣) Yuanjie Zhang(张元杰), and Zhihuang Luo(罗智煌)

Citation: Chin. Phys. B, 2025, 34 (**11**): 110304. DOI: 10.1088/1674-1056/addcc1
http://cpb.iphy.ac.cn; http://iopscience.iop.org/cpb

What follows is a list of articles you may be interested in

Bayesian phase difference estimation based on single-photon projective measurement

Xu-Hao Yu(余旭豪), Ying Wei(韦颖), Ran Yang(杨然), Wen-Hui Song(宋文慧), Yingning Miao(缪应宁), Wei Zhou(周唯), Xinhui Li(李新慧), Xiaoqin Gao(高小钦), Yan-Xiao Gong(龚彦晓), and Shi-Ning Zhu(祝世宁)
Chin. Phys. B, 2025, 34 (**7**): 070305. DOI: 10.1088/1674-1056/adde33

Micron-resolved quantum precision measurement of magnetic field at the Tesla level

Si-Han An(安思瀚), Shi-Yu Ge(葛仕宇), Wen-Tao Lu(卢文韬), Guo-Bin Chen(陈国彬), Sheng-Kai Xia(夏圣开), Ai-Qing Chen(陈爱庆), Cheng-Kun Wang(王成坤), Lin-Yan Yu(虞林嫣), Zhi-Qiang Zhang(张致强), Yang Wang(汪洋), Gui-Jin Tang(唐贵进), Hua-Fu Cheng(程华富), and Guan-Xiang Du(杜关祥)
Chin. Phys. B, 2024, 33 (**12**): 120305. DOI: 10.1088/1674-1056/ad7e9b

New approach to measuring topological phase transitions utilizing Floquet technology

Xue-Ying Yang(杨雪滢), Wei Wu(吴伟), and Ping-Xing Chen(陈平形)
Chin. Phys. B, 2024, 33 (**9**): 090305. DOI: 10.1088/1674-1056/ad5d94

Approximate constructions of counterdiabatic driving with NMR quantum systems

Hui Zhou(周辉), Xiaoli Dai(代晓莉), Jianpei Geng(耿建培), Yunlan Ji(季云兰), and Xinhua Peng(彭新华)
Chin. Phys. B, 2024, 33 (**9**): 090301. DOI: 10.1088/1674-1056/ad58b2

Nuclear magnetic resonance for quantum computing: Techniques and recent achievements

Tao Xin(辛涛), Bi-Xue Wang(王碧雪), Ke-Ren Li(李可仁), Xiang-Yu Kong(孔祥宇), Shi-Jie Wei(魏世杰), Tao Wang(王涛), Dong Ruan(阮东), Gui-Lu Long(龙桂鲁)
Chin. Phys. B, 2018, 27 (**2**): 020308. DOI: 10.1088/1674-1056/27/2/020308

Observation of topology of non-Hermitian systems without chiral symmetry

Shuo Wang(王硕), Zhengjie Kang(康正杰), Hao Li(李浩), Jiaojiao Li(李姣姣), Yuanjie Zhang(张元杰), and Zhihuang Luo(罗智煌)†

Guangdong Provincial Key Laboratory of Quantum Metrology and Sensing, School of Physics and Astronomy, Sun Yat-Sen University (Zhuhai Campus), Zhuhai 519082, *China*

(Received 4 April 2025; revised manuscript received 12 May 2025; accepted manuscript online 23 May 2025)

Topological invariants are crucial for characterizing topological systems. However, experimentally measuring them presents a significant challenge, especially in non-Hermitian systems where the biorthogonal eigenvectors are often necessary. We propose a general approach for measuring the topological invariants of one-dimensional non-Hermitian systems, which can be derived from the spin textures of right eigenstates. By utilizing a dilation method, we realize a non-Hermitian system without chiral symmetry on a two-qubit nuclear magnetic resonance system and measure the winding number associated with the eigenstates. In addition to examining the topology of the eigenstates, our experiment also reveals the topological structure of the energy band, which differs from that in chiral systems. Our work paves the way for further exploration of complex topological properties in non-Hermitian systems without chiral symmetry.

Keywords: nuclear magnetic resonance, quantum simulation, non-Hermitian system, topological phases

PACS: 03.67.Lx, 03.65.Vf, 05.30.Rt, 76.60.–k

DOI: 10.1088/1674-1056/addcc1 **CSTR:** 32038.14.CPB.addcc1

1. Introduction

Topological phases of matter play a central role in condensed matter physics and fault-tolerant quantum computing.[1–5] Recent studies on topological phases have extended to non-Hermitian systems and attracted a great interest in both theoretical[6–38] and experimental domains.[39–56] Different from the Hermitian systems, non-Hermitian systems exhibit unique properties such as complex eigenvalues,[57] biorthonormal eigenvectors,[58] exceptional points,[10,11,45–47] and non-Hermitian skin effects.[15–18,59] These novel phenomena provide valuable insights into non-Hermitian systems. Due to the global nature, topological invariants such as Chern number and winding number can be employed to characterize different topological phases.[5,60–64] However, non-Hermiticity presents challenges for the realization of non-Hermitian systems and the measurement of topological invariants based on biorthogonal eigenvectors, when the definitions of topological invariants in Hermitian systems generalize to non-Hermitian systems.[23,24] The method for measuring the topological invariants in non-Hermitian systems is urgent and may be a prerequisite for exploring non-Hermitian topological phenomena in experiments.

In the non-Hermitian context, measurements of topological invariants are often associated with the right and left eigenstates, governed by H and $H^\dagger$, respectively. Recent theoretical works proposed that the winding number can be measured through the spin textures in non-Hermitian systems.[35,36] In these methods, both the right and left eigenstates are required, which can impose a burden on experiments, because we must separately implement H and $H^\dagger$ to obtain the evolutions of the right and left eigenstates. On the other hand, it is well established that symmetry is crucial in the study of topological properties.[7–9] For non-Hermitian systems, the topological characteristics differ significantly depending on whether or not chiral symmetry is present.[23,24] However, recent experimental studies have primarily focused on measuring the topological invariants of non-Hermitian systems with chiral symmetry,[39,40] while experimental research on non-chiral systems is still lacking.

In this paper, we report an experimental measurement of the topological invariants in one-dimensional (1D) non-Hermitian systems without chiral symmetry. We employ a dilation method to realize the evolution of a general non-Hermitian system on a two-qubit nuclear magnetic resonance (NMR) system. Starting with a right state of the non-Hermitian Hamiltonian, the dilated system evolves under the Hermitian Hamiltonian. We observe the time evolutions of right-state spin textures for a non-Hermitian system through the projection measurement onto the dilated system. We propose a method to measure the winding number of a non-Hermitian system using the right-eigenstate spin textures. The right-eigenstate spin textures and related complex eigenvalues can be extracted by fitting the observed time evolutions of right-state spin textures. Using this approach, the experiment only requires the evolution under H, without the simu-

†Corresponding author. E-mail: luozhih5@mail.sysu.edu.cn

© 2025 Chinese Physical Society and IOP Publishing Ltd. All rights, including for text and data mining, AI training, and similar technologies, are reserved.

lation of $H^\dagger$. Furthermore, we demonstrate that when the chiral symmetry of a non-Hermitian Hamiltonian is broken, the topological invariants of its eigenstates and eigenvalues exhibit different phase transition boundaries.[23] This contrasts with systems possessing chiral symmetry, where the boundaries of both coincide.[24]

2. Theory

The Hamiltonian of a 1D two-band non-Hermitian system can generally be expressed as

$$H(k) = \boldsymbol{h}(k)\cdot\boldsymbol{\sigma}, \tag{1}$$

where $\boldsymbol{h}(k) = (h_x(k), h_y(k), h_z(k))$ is a complex vector field that depends on the quasimomentum k, and $\boldsymbol{\sigma} = (\sigma_x, \sigma_y, \sigma_z)$ denotes the Pauli matrices. Noting that if $h_z = 0$, the Hamiltonian (1) exhibits chiral symmetry, i.e., $\sigma_z H(k)\sigma_z = -H(k)$. However, when $h_z \neq 0$, the Hamiltonian (1) breaks chiral symmetry. Due to the non-Hermiticity of the system, $H(k) \neq H^\dagger(k)$, the distinct right and left eigenstates are defined by $H(k)|\varphi_\mu^{\mathrm{R}}(k)\rangle = E_\mu(k)|\varphi_\mu^{\mathrm{R}}(k)\rangle$ and $H^\dagger(k)|\varphi_\mu^{\mathrm{L}}(k)\rangle = E_\mu^*(k)|\varphi_\mu^{\mathrm{L}}(k)\rangle$, respectively. Here $E_\mu(k) = \mu\sqrt{h_x^2(k)+h_y^2(k)+h_z^2(k)}$ are the complex eigenvalues, with $\mu = \pm$ indexing the two bands. In constract to Hermitian systems, neither $|\varphi_\mu^{\mathrm{R}}(k)\rangle$ nor $|\varphi_\mu^{\mathrm{L}}(k)\rangle$ form an orthogonal basis. Instead, they combine to create a pair of biorthogonal vectors that satisfy: $\langle\varphi_\mu^{\mathrm{L}}(k)|\varphi_{\mu'}^{\mathrm{R}}(k)\rangle = \delta_{\mu\mu'}$ and $\sum_\mu |\varphi_\mu^{\mathrm{R}}(k)\rangle\langle\varphi_\mu^{\mathrm{L}}(k)| = 1$ by the normalization.[58] The explicit forms of the right and left biorthogonal eigenstates of the Hamiltonian (1) are given by

$$\begin{aligned}|\varphi_\mu^{\mathrm{R}}(k)\rangle &= \frac{1}{\sqrt{2E_\mu(E_\mu - h_z)}}(h_x - \mathrm{i}h_y,\ E_\mu - h_z)^{\mathrm{T}},\\ \langle\varphi_\mu^{\mathrm{L}}(k)| &= \frac{1}{\sqrt{2E_\mu(E_\mu - h_z)}}(h_x + \mathrm{i}h_y,\ E_\mu - h_z).\end{aligned} \tag{2}$$

If the system starts at an initial right state $|\psi^{\mathrm{R}}(k,0)\rangle = \sum_\mu c_\mu|\varphi_\mu^{\mathrm{R}}(k)\rangle$ or its related left state $\langle\psi^{\mathrm{L}}(k,0)| = \sum_\mu c_\mu^*\langle\varphi_\mu^{\mathrm{L}}(k)|$, their time evolutions governed by $H(k)$ and $H^\dagger(k)$ are described by

$$\begin{aligned}|\psi^{\mathrm{R}}(k,t)\rangle &= \sum_\mu c_\mu(k)\,\mathrm{e}^{-\mathrm{i}E_\mu(k)t}|\varphi_\mu^{\mathrm{R}}(k)\rangle,\\ \langle\psi^{\mathrm{L}}(k,t)| &= \sum_\mu c_\mu^*(k)\,\mathrm{e}^{\mathrm{i}E_\mu^*(k)t}\langle\varphi_\mu^{\mathrm{L}}(k)|.\end{aligned} \tag{3}$$

To characterize the properties of non-Hermitian systems, it is essential to consider the topological invariants, such as the winding number. One can readily generalize the definition of winding number that is related to the Berry phase in Hermitian systems to non-Hermitian systems, which can be written as[24,30]

$$w_\mu = \frac{1}{\pi}\oint \mathrm{d}k\langle\varphi_\mu^{\mathrm{L}}(k)|\mathrm{i}\partial_k|\varphi_\mu^{\mathrm{R}}(k)\rangle, \tag{4}$$

where $\mu = \pm$ indicates the band labels. For Hermitian systems, we have $|\varphi_\mu^{\mathrm{L}}(k)\rangle = |\varphi_\mu^{\mathrm{R}}(k)\rangle$, whereas in non-Hermitian systems, $|\varphi_\mu^{\mathrm{L}}(k)\rangle \neq |\varphi_\mu^{\mathrm{R}}(k)\rangle$, making it challenging to detect w_μ in experiments.

By substituting the explicit forms of $|\varphi_\mu^{\mathrm{R}}(k)\rangle$ and $\langle\varphi_\mu^{\mathrm{L}}(k)|$ into Eq. (4), we represent w_μ as follows:

$$w_\mu = \frac{1}{2\pi}\oint_S \mathrm{d}k\frac{h_x\partial_k h_y - h_y\partial_k h_x}{E_\mu(E_\mu - h_z)}. \tag{5}$$

For the case of chiral symmetry (i.e., $h_z = 0$), it can be found that the w_μ for each band takes the same value, i.e., $w_+ = w_-$. But for the general case without chiral symmetry, w_μ is not a quantized number and $w_+ \neq w_-$, showing that w_μ is no longer topological-invariant. Nevertheless, their sum

$$w_t = w_+ + w_- = \frac{1}{\pi}\oint_S \partial_k\phi_{yx}\mathrm{d}k \tag{6}$$

has been demonstrated to be a topological invariant,[24] where $\phi_{yx} = \arctan(h_y/h_x)$ is a complex angle.

We can use w_t to distinguish topological phases in systems without chiral symmetry. Since $\mathrm{Im}(\phi_{yx})$ is a real continuous periodic function of k, we have $\oint_{\mathrm{c}}\partial_k\mathrm{Im}(\phi_{yx})\mathrm{d}k = 0$, which means that only $\mathrm{Re}(\phi_{yx})$ contributes to the integral of Eq. (6).

To measure the winding number w_t, recent theoretical work[35] demonstrated that the real part of ϕ_{yx} can be decomposed as

$$\mathrm{Re}[\phi_{yx}(k)] = \frac{1}{2}\left[\phi_{yx}^{\mathrm{RR}}(k) + \phi_{yx}^{\mathrm{LL}}(k)\right] + n\frac{\pi}{2}, \tag{7}$$

where n is an integer, and

$$\phi_{yx}^{\beta\beta} = \arctan\left(\frac{\overline{\langle\psi^\beta(k,t)|\sigma_y|\psi^\beta(k,t)\rangle}}{\overline{\langle\psi^\beta(k,t)|\sigma_x|\psi^\beta(k,t)\rangle}}\right) \tag{8}$$

with $\beta = \mathrm{R}$, and L, and the long-time average of spin texture is defined as

$$\begin{aligned}&\overline{\langle\psi^\beta(k,t)|\sigma_\alpha|\psi^\beta(k,t)\rangle}\\ &= \lim_{T\to\infty}\frac{1}{T}\int_0^T\frac{\langle\psi^\beta(k,t)|\sigma_\alpha|\psi^\beta(k,t)\rangle}{\langle\psi^\beta(k,t)|\psi^\beta(k,t)\rangle}\mathrm{d}t,\\ &(\alpha = x,y,z).\end{aligned} \tag{9}$$

Since the spin textures are observable, equation (7) implies that the winding number w_t of a non-Hermitian system can be experimentally detected from ϕ_{yx}^{RR} and ϕ_{yx}^{LL}, which are related to the dynamics of the right and left states governed by $H(k)$ and $H^\dagger(k)$, respectively. Consequently, it is insufficient to extract w_t from the time evolution of either $H(k)$ or $H^\dagger(k)$ alone. Furthermore, the realization of $H^\dagger(k)$ presents a practical obstacle in the experiment.

Similarly, $\mathrm{Re}(\phi_{yx})$ can be rewritten in another way (see the proof in Appendix A)

$$\mathrm{Re}[\phi_{yx}(k)] = \frac{1}{2}\left[\phi_{yx}^{++}(k) + \phi_{yx}^{--}(k)\right] + n\frac{\pi}{2}, \tag{10}$$

where

$$\phi_{yx}^{\mu\mu}(k) = \arctan\left(\frac{\langle\varphi_\mu^{\mathrm{R}}(k)|\sigma_y|\varphi_\mu^{\mathrm{R}}(k)\rangle}{\langle\varphi_\mu^{\mathrm{R}}(k)|\sigma_x|\varphi_\mu^{\mathrm{R}}(k)\rangle}\right) \tag{11}$$

with $\mu = \pm$. Figure 1 shows different results of Eqs. (7)–(11), where we take an example with $h_x = J_0 + J_1\cos(k) + J_2\cos(2k)$, $h_y = J_1\sin(k) + J_2\sin(2k) - \mathrm{i}\delta$, and $h_z = 0.5$. The parameters are set to $J_0 = 3, J_{1,2} = 1$, $\delta = 0.3$ for Figs. 1(a), 1(c), and 1(e) with $w_t = 0$, and $J_{0,1,2} = 1$, $\delta = 0.3$ for Figs. 1(b), 1(d), and 1(f) with $w_t = 2$. Though ϕ_{yx}^{++} and ϕ_{yx}^{--} in Fig. 1(d) are different from ϕ_{yx}^{RR} and ϕ_{yx}^{LL} in Fig. 1(b), the averages of them are the same with the theoretical value of $\mathrm{Re}[\phi_{yx}]$, as shown in Fig. 1(f). Based on the above results, $\mathrm{Re}[\phi_{yx}(k)]$ can be obtained solely from the right–right spin textures $\langle\varphi_\pm^{\mathrm{R}}(k)|\sigma_\alpha|\varphi_\pm^{\mathrm{R}}(k)\rangle$ ($\alpha = x, y$), whose dynamics are determined by only $H(k)$. This simplifies the process of measuring the winding number w_t of a general non-Hermitian Hamiltonian (1) in experiments, as there is no longer a need to implement the $H^\dagger(k)$. Both $\langle\varphi_\pm^{\mathrm{R}}(k)|\sigma_\alpha|\varphi_\pm^{\mathrm{R}}(k)\rangle$ for $\alpha = x$ or y can be obtained simultaneously by fitting the time evolution of spin textures $\langle\psi^{\mathrm{R}}(k,t)|\sigma_\alpha|\psi^{\mathrm{R}}(k,t)\rangle$, if $c_\pm \neq 0$ (see Section 4 for more details).

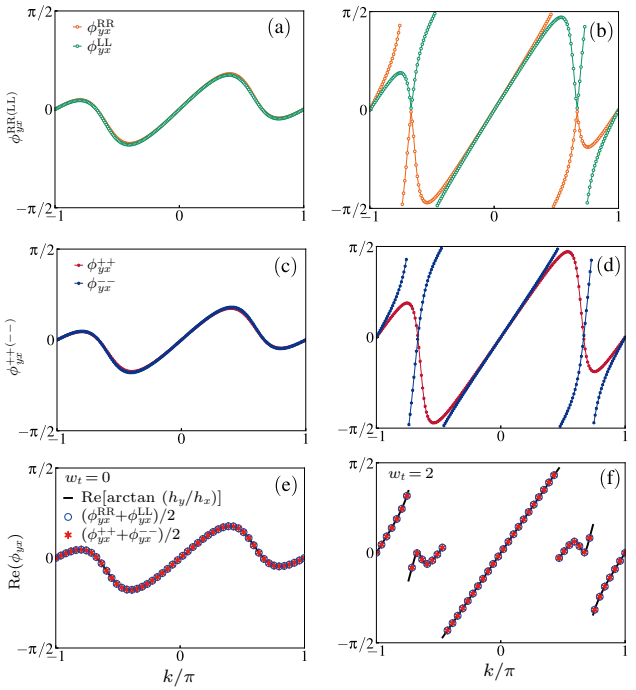


Fig. 1. (a)–(b) ϕ_{yx}^{RR} and ϕ_{yx}^{LL} as a function of k, calculated from the long time average of right–right and left–left spin textures. (c)–(d) ϕ_{yx}^{++} and ϕ_{yx}^{--} as a function of k, computed from the spin textures of the two right eigenstates. (e)–(f) $\mathrm{Re}(\phi_{yx})$, defined by $\phi_{yx} \equiv \mathrm{actan}(h_y/h_x)$, is equal to $(\phi_{yx}^{\mathrm{RR}} + \phi_{yx}^{\mathrm{LL}})/2$ and $(\phi_{yx}^{++} + \phi_{yx}^{--})/2$. Here parameters are set to $J_0 = 3, J_{1,2} = 1$, $\delta = 0.3$ with $w_t = 0$ (left panel) and $J_0 = 1, J_{1,2} = 1$, $\delta = 0.3$ with $w_t = 2$ (right panel).

3. Experiment

The experiment is performed on a Bruker AVANCE 300 MHz spectrometer with a 2-qubit sample ^{13}C-labeled chloroform dissolved in acetone-d6, whose molecular structure and Hamiltonian parameters are illustrated in Fig. 2(a). Its NMR Hamiltonian in a rotating frame is

$$H_{\mathrm{NMR}} = -\sum_i^2 \pi(\nu_i - \nu_i^{\mathrm{RF}})\sigma_z^i + \frac{\pi J}{2}\sigma_z^1\sigma_z^2. \tag{12}$$

Here ν_i and ν_i^{RF} ($i = 1, 2$) represent the chemical shifts and the reference frequencies of radio-frequency (RF) fields, and the J is the coupling strength between ^{13}C and ^{1}H. Each nuclear spin can be individually controlled by RF pulses. The corresponding control Hamiltonian reads

$$H_{\mathrm{c}} = \sum_{i=1}^2 \pi B_i(\cos\Phi_i\sigma_x^i + \sin\Phi_i\sigma_y^i), \tag{13}$$

where B_i and Φ_i are amplitudes and phases of the RF fields. By tuning the control parameters B_i and Φ_i of RF fields, we can simulate the dynamical evolution of a general two-qubit system.

We consider a non-Hermitian Hamiltonian (1) with a complex vector field

$$h_x = J_0 + J_1\cos(k), \quad h_y = J_1\sin(k) - \mathrm{i}\delta, \quad h_z = 0.5. \tag{14}$$

It is a nonchiral system because of $h_z \neq 0$. The phase diagram exhibits two different topological phases with $w_t = 1$ for $J_0 = 1$, $J_1 = 1$, $\delta = 0.3$, and $w_t = 2$ when $J_0 = 0.3$, $J_1 = 1$, $\delta = 0.3$. To implement the non-Hermitian Hamiltonian in the experiment, we exploit a dilation method.[47,65] The dilated Hermitian Hamiltonian obtained from the non-Hermitian Hamiltonian (1) can be expressed as

$$H_{\mathrm{s,a}}(t) = \Lambda(t)\otimes I + \Gamma(t)\otimes\sigma_z, \tag{15}$$

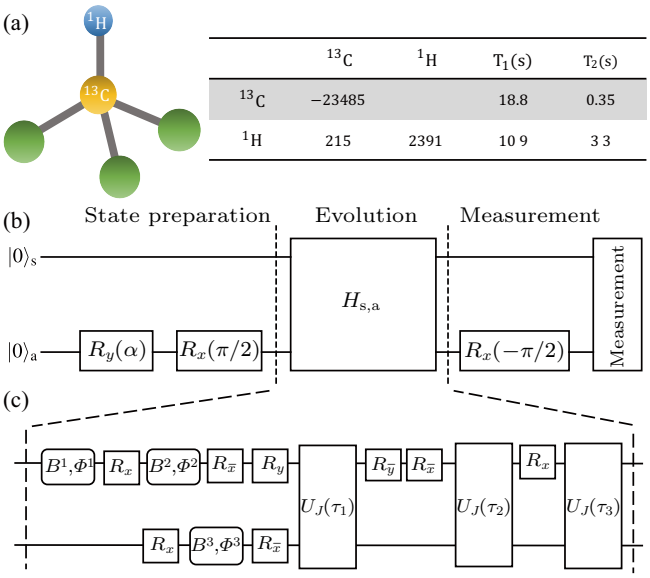
where $\Lambda(t) = \sum_{\alpha=0}^3 \lambda_\alpha(t)\sigma_\alpha$ and $\Gamma(t) = \sum_{\alpha=0}^3 \gamma_\alpha(t)\sigma_\alpha$, and σ_0 denotes the identity operator I. The coefficients of λ_α and γ_α can be found in Appendix B. By introducing an ancillary qubit, the dilated state evolves as

$$|\Psi(k,t)\rangle_{\mathrm{s,a}} = |\psi^{\mathrm{R}}(k,t)\rangle_{\mathrm{s}}|-\rangle_{\mathrm{a}} + \eta(t)|\psi^{\mathrm{R}}(k,t)\rangle_{\mathrm{s}}|+\rangle_{\mathrm{a}}, \tag{16}$$

under the $H_{\mathrm{s,a}}(t)$, where $|\psi^{\mathrm{R}}(k,t)\rangle_{\mathrm{s}}$ is the right state of the non-Hermitian system (see Eq. (3)), $|\pm\rangle_{\mathrm{a}}$ are eigenstates of σ_y of the ancillary qubit and $\eta(t)$ is an appropriate linear operator.[47,65]

Figure 2(a) shows the quantum circuit for realizing the dynamical evolution of the non-Hermitian Hamiltonian using the dilation method. Starting with the initial state: $|0\rangle_{\mathrm{s}}|0\rangle_{\mathrm{a}}$, the system is prepared to the dilated state: $|\Psi(k,0)\rangle_{\mathrm{s,a}} = |\psi^{\mathrm{R}}(k,0)\rangle_{\mathrm{s}}|-\rangle_{\mathrm{a}} + \eta(0)|\psi^{\mathrm{R}}(k,0)\rangle_{\mathrm{s}}|+\rangle_{\mathrm{a}}$ by two single-qubit rotations $R_y(\alpha)$ ($\alpha = 2\arctan\eta_0$) along the y direction and $R_x(\pi/2)$ along the x direction acting the ancillary qubit, and evolves under the dilated Hermitian Hamiltonian $H_{\mathrm{s,a}}$, which can be implemented by pulse sequence of Fig. 2(c). After an $R_x(-\pi/2)$, the final state of the dilated system is

$$|\Psi(k,t)\rangle_{\mathrm{s,a}}^{\mathrm{f}} = |\psi^{\mathrm{R}}(k,t)\rangle_{\mathrm{s}}|0\rangle_{\mathrm{a}} + \eta(t)|\psi^{\mathrm{R}}(k,t)\rangle_{\mathrm{s}}|1\rangle_{\mathrm{a}}. \tag{17}$$



	^{13}C	^{1}H	T_1(s)	T_2(s)
^{13}C	−23485		18.8	0.35
^{1}H	215	2391	10 9	3 3

Fig. 2. (a) Molecular structure of ^{13}C-labeled chloroform consisting of ^{13}C and ^{1}H nuclear spins, and its Hamiltonian parameters. The diagonal and off-diagonal elements represent the chemical shifts and J-coupling constants (in unit Hz). The T_1 and T_2 are spin–lattice relaxation times and spin–spin relaxation times (in unit seconds). (b) Quantum circuit for realizing the dynamical evolution of a general non-Hermitian system using the dilation method. The ^{13}C and ^{1}H are used as the system qubit and ancillary qubit, respectively. $R_y(\alpha)$ denotes the single-qubit rotation α along the y direction, with $\alpha = 2\arctan\eta_0$. (c) Pulse sequence for realizing the dilated Hamiltonian $H_{s,a}$. B^i and Φ^i $(i = 1,2,3)$ given by Appendix B represent the amplitudes and phases of the control Hamiltonian (13), $U_J(\tau_j) = \exp[-\mathrm{i}\frac{\pi J}{2}\sigma_z^1\sigma_z^2\tau_j]$ is the free evolution of the NMR Hamiltonian (12), where we set $\nu_i^{\mathrm{RF}} = \nu_i$ in our experiment, and $\tau_j = 2\gamma_j(t_{\mathrm{m}})\tau/\pi J$.

Thus, we can obtain the time evolution of the right state $|\psi_{\mathrm{s}}^{\mathrm{R}}(t)\rangle$ by projecting onto the $|0\rangle_{\mathrm{a}}\langle 0|$ subspace. In experiments, we employ the gradient ascent pulse engineering (GRAPE) technique[66] to optimize the quantum circuit in Fig. 2(b) with high precision. The observable operators $\sigma_\alpha \otimes |0\rangle_{\mathrm{a}}\langle 0|$ with $\alpha = x,y$ are chosen for the measurements of $\langle\psi^{\mathrm{R}}(k,t)|\sigma_\alpha|\psi^{\mathrm{R}}(k,t)\rangle = \sum_{\mu,\mu'}^{\pm} c_\mu^* c_{\mu'}\, \mathrm{e}^{\mathrm{i}(E_\mu^* - E_{\mu'})t}\langle\varphi_\mu^{\mathrm{R}}|\sigma_\alpha|\varphi_{\mu'}^{\mathrm{R}}\rangle$. We model the time evolution of the spin texture

$$\begin{aligned}
&\langle\psi^{\mathrm{R}}(k,t)|\sigma_\alpha|\psi^{\mathrm{R}}(k,t)\rangle \\
=\ & |c_+|^2\langle\psi_+^{\mathrm{R}}(k)|\sigma_\alpha|\psi_+^{\mathrm{R}}(k)\rangle\,\mathrm{e}^{2\mathrm{Im}(E_+)t} \\
&+ |c_-|^2\langle\psi_-^{\mathrm{R}}(k)|\sigma_\alpha|\psi_-^{\mathrm{R}}(k)\rangle\,\mathrm{e}^{2\mathrm{Im}(E_-)t} \\
&+ c_+^* c_-\langle\psi_+^{\mathrm{R}}(k)|\sigma_\alpha|\psi_-^{\mathrm{R}}(k)\rangle\,\mathrm{e}^{\mathrm{i}2\mathrm{Re}(E_+)t} \\
&+ c_-^* c_+\langle\psi_-^{\mathrm{R}}(k)|\sigma_\alpha|\psi_+^{\mathrm{R}}(k)\rangle\,\mathrm{e}^{\mathrm{i}2\mathrm{Re}(E_-)t}
\end{aligned}$$

as a fitting function. This expression includes two decaying terms and two oscillatory terms. The decay is controlled by the imaginary parts of the eigenvalues, while the oscillations are governed by their real parts. The amplitudes reflect the eigenstate spin textures. If the initial state $|\psi^{\mathrm{R}}(k,0)\rangle = \sum_\mu^{\pm} c_\mu|\varphi_\mu^{\mathrm{R}}\rangle$ is prepared to satisfy that $c_\pm \neq 0$, we can extract both the eigenstate spin texture components and the real and imaginary parts of the complex eigenvalues by fitting this function. Here, we emphasize that the values of the eigenstate spin textures are obtained in the form of $|c_\mu|^2|\langle\psi_\mu|\sigma_\alpha|\psi_\mu\rangle$ (where $\mu = \pm$). But this does not affect the measurement of $\mathrm{Re}[\phi_{yx}(k)]$), since

$$\frac{|c_\mu|^2\langle\psi_\mu^{\mathrm{R}}(k)|\sigma_y|\psi_\mu^{\mathrm{R}}(k)\rangle}{|c_\mu|^2\langle\psi_\mu^{\mathrm{R}}(k)|\sigma_x|\psi_\mu^{\mathrm{R}}(k)\rangle} = \frac{\langle\psi_\mu^{\mathrm{R}}(k)|\sigma_y|\psi_\mu^{\mathrm{R}}(k)\rangle}{\langle\psi_\mu^{\mathrm{R}}(k)|\sigma_x|\psi_\mu^{\mathrm{R}}(k)\rangle}, \tag{18}$$

when we use the same initial state.

4. Results

Figures 3(a) and 3(b) show the time evolutions of spin textures $\langle\psi^{\mathrm{R}}(k,t)|\sigma_\alpha|\psi^{\mathrm{R}}(k,t)\rangle$ for $\alpha = x,y$ and $k = -0.448\pi$. Here, the non-Hermitian Hamiltonian parameters were taken as $J_0 = 1$, $J_1 = 1$, $\delta = 0.3$, corresponding to the winding number $w_t = 1$. The experimental results are in agreement with the theoretical predictions, confirming that the dilated method for simulating the dynamical evolution of the non-Hermitian Hamiltonian (1) is feasible in the experiment. From the fitting results of Figs. 3(a) and 3(b), the eigenstate spin textures $\langle\sigma_\alpha\rangle_\pm = \langle\varphi_\pm^{\mathrm{R}}(k)|\sigma_\alpha|\varphi_\pm^{\mathrm{R}}(k)$ for $\alpha = x,y$ were extracted, as presented in Fig. 3(c). We now get a measured data point of $\mathrm{Re}[\phi_{yx}(k)]$ for $k = -0.448\pi$, according to Eqs. (10) and (11). Also, we obtained the real and imaginary parts of the eigenvalues depicted in Fig. 3(d), from the fitting results.

Using the same method above, we measured $\mathrm{Re}[\phi_{yx}(k)]$ for $k \in [-\pi,\pi]$. The winding number w_t is computed as the integral of a piecewise-defined function

$$\begin{aligned}
w_t = \frac{1}{\pi}\Bigg(&\int_{-\pi}^{k_1}\partial_k\mathrm{Re}[\phi_{yx}(k)]\,\mathrm{d}k + \int_{k_1}^{k_2}\partial_k\mathrm{Re}[\phi_{yx}(k)]\,\mathrm{d}k \\
&+ \int_{k_2}^{\pi}\partial_k\mathrm{Re}[\phi_{yx}(k)]\,\mathrm{d}k\Bigg),
\end{aligned} \tag{19}$$

where k_1 and k_2 denote the points of discontinuity. The results of two distinct topological phases with $w_t = 1$ and $w_t = 2$ are shown in Figs. 3(e) and 3(f), respectively. From these results, it is evident that we successfully measured the topological invariants w_t of a non-Hermitian Hamiltonian that breaks chiral symmetry, without the need of the left states whose dynamical evolutions are governed by $H^\dagger$.

In addition to the nontrivial topology of the eigenstates, the topological structures of the energy bands were also observed. The eigenvalues of a non-Hermitian Hamiltonian are generally complex, and its band structures also exhibit topological properties, which can be described by another winding number ν_{E},[12,13]

$$\nu_{\mathrm{E}} = \sum_\mu^{\pm}\int_{-\pi}^{\pi}\frac{\mathrm{d}k}{2\pi}\partial_k\arg E_\mu(k), \tag{20}$$

where $\arg E_\mu(k)$ is the argument of the complex energy $E_\mu(k) = \mu\sqrt{1 + J_0^2 - \delta^2 + h_z^2 + 2J_0\cos k - \mathrm{i}2\delta\sin k}$. Figures 3(g) and 3(h) show the band structures of our model with both $\nu_{\mathrm{E}} = 0$, as the projections of the energy bands on the complex energy plane form two separate circles that do not

wind around the origin. It is worth noting that there are no band-touching points, implying the absence of a phase transition, which is different from the results with nonzero winding numbers w_ts corresponding to two distinct topological phases.

In contrast to chiral systems, the phase boundaries characterized by w_t and ν_{E} coincide.[23] However, in the absence of the chiral symmetry, the phase boundaries of ν_{E} correspond to the band-touching points of the non-chiral system, but no band touching occurs at the phase boundaries of w_t. This is quite different from the chiral non-Hermitian Hamiltonian; see Appendix E for more details. Our experiments exhibit the unusual phenomenon of a non-chiral system by measuring both eigenstate topological invariant w_t and eigenvalue topological invariant ν_{E}. The error analysis can be found in Appendix D.

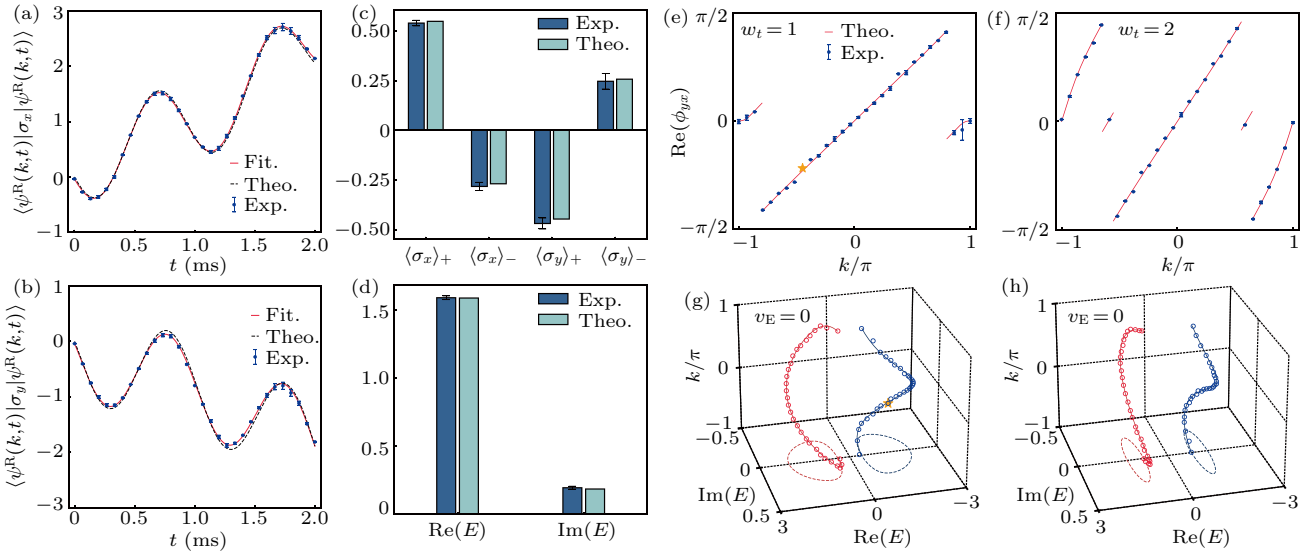


Fig. 3. (a)–(b) Time evolutions of spin textures $\langle\psi^{\mathrm{R}}(k,t)|\sigma_\alpha|\psi^{\mathrm{R}}(k,t)\rangle$ for $\alpha = x,y$, and $k = -0.448\pi$, corresponding to the points labeled by orange stars in panels (e) and (g). (c) Eigenstate spin textures $\langle\sigma_\alpha\rangle_\pm = \langle\varphi^{\mathrm{R}}_\pm(k)|\sigma_\alpha|\varphi^{\mathrm{R}}_\pm(k)$ for $\alpha = x$ and y, obtained by fitting the curves of panels (a) and (b), respectively. (d) Real and imaginary parts of the complex eigenvalue E, resulted from the same fitting procedure. (e)–(f) $\mathrm{Re}(\phi)_{yx}$ as a function of k with $w_t = 1$ and $w_t = 2$. (g)–(h) $\mathrm{Re}(E)$ and $\mathrm{Im}(E)$ as a function of k with $\nu_{\mathrm{E}} = 0$. Parameters are chosen as $J_0 = 1, J_1 = 1, \delta = 0.3$ for panels (e) and (g), and $J_0 = 0.3, J_1 = 1, \delta = 0.3$ for panels (f) and (h), respectively.

5. Conclusion

We presented a general scheme for measuring the winding numbers of 1D non-Hermitian systems. Unlike previous works,[35,36] our approach does not rely on left eigenstates governed by $H^\dagger$, offering an experimental advantage. By employing the dilated method,[40,65] we realized a non-Hermitian system without chiral symmetry on a two-qubit NMR system and measured the winding numbers using our scheme, where the right-eigenstate spin textures of two bands were simultaneously extracted by fitting the observed time evolutions of spin textures. Meanwhile, we also obtained the complex eigenvalues for two distinct topological phases from the same fitting procedure. Our experimental results demonstrated a discrepancy between the phase boundaries of phase diagrams characterized by the two independent topological invariants w_t and ν_{E}, due to the breaking of chiral symmetry. In future work, extending our scheme to explore the topology of higher-dimensional non-Hermitian models, such as measuring Chern numbers in two-dimensional systems, would be particularly interesting but also experimentally challenging, because of the extensive spin textures to be measured in high dimensional systems.

Appendix A: Relations between azimuthal angle and eigenstate spin textures

According to Eq. (2), the right eigenstates of Hamiltonian (1) can also be rewritten as

$$|\varphi^{\mathrm{R}}_+\rangle = \left(\mathrm{e}^{-\mathrm{i}\phi_{yx}}\cos\frac{\beta}{2}, \sin\frac{\beta}{2}\right)^{\mathrm{T}},$$
$$|\varphi^{\mathrm{R}}_-\rangle = \left(\mathrm{e}^{-\mathrm{i}\phi_{yx}}\sin\frac{\beta}{2}, -\cos\frac{\beta}{2}\right)^{\mathrm{T}}, \tag{A1}$$

where

$$\cos\beta = \frac{h_z}{\sqrt{h_x^2+h_y^2+h_z^2}}, \quad \mathrm{e}^{\mathrm{i}\phi_{yx}} = \frac{h_x+\mathrm{i}h_y}{\sqrt{h_x^2+h_y^2}}. \tag{A2}$$

Here $\phi_{yx} = \arctan(h_y/h_x)$ is the azimuthal angle discussed in the main text. We first define the quantity $\phi^{\mu\mu}_{yx}$ ($\mu = \pm$) that satisfy

$$\tan\phi^{\mu\mu}_{yx} \equiv \frac{\langle\varphi^{\mathrm{R}}_\mu|\sigma_y|\varphi^{\mathrm{R}}_\mu\rangle}{\langle\varphi^{\mathrm{R}}_\mu|\sigma_x|\varphi^{\mathrm{R}}_\mu\rangle}. \tag{A3}$$

By substituting Eqs. (A1) and (A2) into Eq. (A3), we can obtain

$$\tan\phi^{++}_{yx} = \mathrm{i}\frac{\mathrm{e}^{-\mathrm{i}\phi_{yx}}\mathcal{S}^* - \mathrm{e}^{\mathrm{i}\phi^*_{yx}}\mathcal{S}}{\mathrm{e}^{-\mathrm{i}\phi_{yx}}\mathcal{S}^* + \mathrm{e}^{\mathrm{i}\phi^*_{yx}}\mathcal{S}},$$

$$\tan\phi_{yx}^{--} = \mathrm{i}\frac{\mathrm{e}^{-\mathrm{i}\phi_{yx}}\mathcal{S} - \mathrm{e}^{\mathrm{i}\phi_{yx}^*}\mathcal{S}^*}{\mathrm{e}^{-\mathrm{i}\phi_{yx}}\mathcal{S} + \mathrm{e}^{\mathrm{i}\phi_{yx}^*}\mathcal{S}^*} \tag{A4}$$

with $\mathcal{S} = \sin(\beta/2)\cos(\beta^*/2)$. Therefore, we have

$$\begin{aligned}\tan(\phi_{yx}^{++} + \phi_{yx}^{--}) &= \frac{\tan\phi_{yx}^{++} + \tan\phi_{yx}^{--}}{1 - \tan\phi_{yx}^{++}\tan\phi_{yx}^{--}} \\ &= \mathrm{i}\frac{\mathrm{e}^{-\mathrm{i}2\phi_{yx}} - \mathrm{e}^{\mathrm{i}2\phi_{yx}^*}}{\mathrm{e}^{-\mathrm{i}2\phi_{yx}} + \mathrm{e}^{\mathrm{i}2\phi_{yx}^*}} \\ &= \tan[2\mathrm{Re}(\phi_{yx})],\end{aligned} \tag{A5}$$

and it is easy to derive the relationship of Eq. (11) in the main text, i.e.,

$$\mathrm{Re}(\phi_{yx}) = \frac{1}{2}(\phi_{yx}^{++} + \phi_{yx}^{--}) + \frac{n\pi}{2}. \tag{A6}$$

Note that only the right eigenstates have been used in the above derivation.

For the left eigenstates,

$$\begin{aligned}\langle\psi_+^{\mathrm{L}}| &= \left(\mathrm{e}^{\mathrm{i}\phi_{yx}}\cos\frac{\beta}{2}, \sin\frac{\beta}{2}\right), \\ \langle\psi_-^{\mathrm{L}}| &= \left(\mathrm{e}^{\mathrm{i}\phi_{yx}}\sin\frac{\beta}{2}, -\cos\frac{\beta}{2}\right),\end{aligned} \tag{A7}$$

we arrive at the same result as above by following a similar procedure, where

$$\tan\phi_{yx}^{\mu\mu} \equiv \frac{\langle\varphi_\mu^{\mathrm{L}}|\sigma_y|\varphi_\mu^{\mathrm{L}}\rangle}{\langle\varphi_\mu^{\mathrm{L}}|\sigma_x|\varphi_\mu^{\mathrm{L}}\rangle}. \tag{A8}$$

On the other hand, ϕ_{yx} can be directly obtained by simultaneously using both the left and right eigenstates,

$$\tan\phi_{yx} \equiv \frac{\langle\varphi_\mu^{\mathrm{L}}|\sigma_y|\varphi_\mu^{\mathrm{R}}\rangle}{\langle\varphi_\mu^{\mathrm{L}}|\sigma_x|\varphi_\mu^{\mathrm{R}}\rangle}. \tag{A9}$$

Here, $\phi_{yx} = \arctan(h_y/h_x)$ is a complex-valued angle, and $\langle\varphi_\mu^{\mathrm{L}}|\sigma_{x,y}|\varphi_\mu^{\mathrm{R}}\rangle$ are not directly accessible through measurement.

Appendix B: The dilated method for realizing a non-Hermitian system

To implement a non-Hermitian Hamiltonian in the experiment, we exploit the dilation method.[47,65] The Hermitian Hamiltonian dilated by an ancillary qubit can be expressed as

$$H_{\mathrm{s,a}}(t) = \Lambda(t)\otimes I + \Gamma(t)\otimes\sigma_z \tag{B1}$$

with

$$\begin{aligned}\Lambda(t) &= \{H_{\mathrm{s}}(t) + \left[\mathrm{i}\frac{\mathrm{d}}{\mathrm{d}t}\eta(t) + \eta(t)H_{\mathrm{s}}(t)\right]\eta(t)\}M^{-1}(t), \\ \Gamma(t) &= \mathrm{i}\left[H_{\mathrm{s}}(t)\eta(t) - \eta(t)H_{\mathrm{s}}(t) - \mathrm{i}\frac{\mathrm{d}}{\mathrm{d}t}\eta(t)\right]M^{-1}(t).\end{aligned} \tag{B2}$$

Here $H_{\mathrm{s}}(t)$ is the Hamitonian of non-Hermitian system, $M(t) = \mathcal{T}\mathrm{e}^{-\mathrm{i}\int_0^t H_{\mathrm{s}}^\dagger(t)\,\mathrm{d}t}M(0)\bar{\mathcal{T}}\mathrm{e}^{\mathrm{i}\int_0^t H_{\mathrm{s}}(t)\,\mathrm{d}t}$, and $\eta(t) = \sqrt{M(t)-I}$, where $\mathcal{T}$ is time-ordering operator ($\hbar$ is set to 1 for simplicity), $M(0) = (\eta_0^2+1)I$, η_0 needs to be set appropriately to keep $M(t)-I$ positive for all t, and I is identity operator. Considering a general 1D two-band non-Hermitian Hamiltonian (1), the dilated Hamiltonian can be expanded in terms of Pauli operators:

$$H_{\mathrm{s,a}}(k,t) = \sum_{\alpha=1}^{4}\lambda_\alpha(k,t)\sigma_\alpha^{\mathrm{s}}\otimes I^{\mathrm{a}} + \sum_{\alpha=1}^{4}\gamma_\alpha(k,t)\sigma_\alpha^{\mathrm{s}}\otimes\sigma_z^{\mathrm{a}}, \tag{B3}$$

where $\lambda_\alpha(k,t)$ and $\gamma_\alpha(k,t)$ ($\alpha = 1,2,3,4$) are real time-dependent control parameters. For the case of $k = -0.448\pi$, the $\lambda_\alpha(k,t)$ and $\gamma_\alpha(k,t)$ for $\alpha = 1,2,3,4$ are illustrated in Fig. B1.

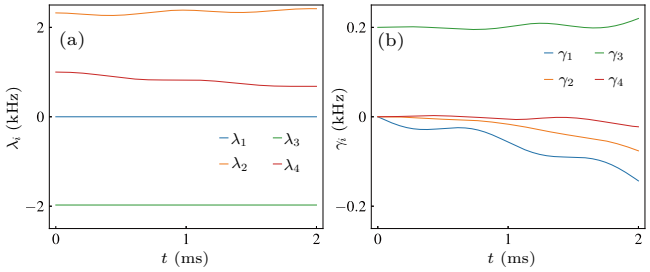


Fig. B1. Time-dependent control parameters $\lambda_\alpha(k,t)$ (a) and $\gamma_\alpha(k,t)$ (b) of the dilated Hermitian Hamiltonian (B3), where $\alpha = 1,2,3,4$, and $k = -0.448\pi$.

We now employ the Trotter approximation formula to realize $H_{\mathrm{s,a}}(k,t)$. The total evolution time T is divided into M time slices with a duration of $\tau = T/M$. The evolution for $t_{\mathrm{m}} = m\tau$ can be approximated to

$$\begin{aligned}\mathrm{e}^{-\mathrm{i}\tau H_{\mathrm{s,a}}(t_{\mathrm{m}})} \approx\ & \mathrm{e}^{-\mathrm{i}\tau[\lambda_2(t_{\mathrm{m}})\sigma_x^{\mathrm{s}} + \lambda_3(t_{\mathrm{m}})\sigma_y^{\mathrm{s}}]}\mathrm{e}^{-\mathrm{i}\tau[\lambda_4(t_{\mathrm{m}})\sigma_z^{\mathrm{s}} + \gamma_1(t_{\mathrm{m}})\sigma_z^{\mathrm{a}}]} \\ & \mathrm{e}^{-\mathrm{i}\tau\gamma_2(t_{\mathrm{m}})\sigma_x^{\mathrm{s}}\sigma_z^{\mathrm{a}}}\mathrm{e}^{-\mathrm{i}\tau\gamma_3(t_{\mathrm{m}})\sigma_y^{\mathrm{s}}\sigma_z^{\mathrm{a}}}\mathrm{e}^{-\mathrm{i}\tau\gamma_4(t_{\mathrm{m}})\sigma_z^{\mathrm{s}}\sigma_z^{\mathrm{a}}}.\end{aligned} \tag{B4}$$

By adjusting the amplitudes and phases of the RF fields (see Eq. (13), i.e.,

$$\begin{aligned}B_{\mathrm{s}}^1 &= \frac{\tau}{\pi}\sqrt{\lambda_2^2(t_{\mathrm{m}}) + \lambda_3^2(t_{\mathrm{m}})}, \\ \Phi_{\mathrm{s}}^1 &= \arccos\left[\lambda_2(t_{\mathrm{m}})/\sqrt{\lambda_2^2(t_{\mathrm{m}}) + \lambda_3^2(t_{\mathrm{m}})}\right],\end{aligned} \tag{B5}$$

we can realize the evolution $\mathrm{e}^{-\mathrm{i}\tau[\lambda_2(t_{\mathrm{m}})\sigma_x^{\mathrm{s}} + \lambda_3(t_{\mathrm{m}})\sigma_y^{\mathrm{s}}]}$. Similarly, we set

$$\begin{aligned}B_{\mathrm{s}}^2 &= \lambda_4(t_{\mathrm{m}})/\pi, \quad \Phi_{\mathrm{s}}^2 = \pi/2, \\ B_{\mathrm{a}}^3 &= \gamma_1(t_{\mathrm{m}})/\pi, \quad \Phi_{\mathrm{a}}^3 = \pi/2,\end{aligned} \tag{B6}$$

to realize the evolutions

$$\begin{aligned}\mathrm{e}^{-\mathrm{i}\tau\lambda_4(t_{\mathrm{m}})\sigma_z^{\mathrm{s}}} &= R_x^{\mathrm{s}}\mathrm{e}^{-\mathrm{i}\pi B_{\mathrm{s}}^2(\cos\Phi_{\mathrm{s}}^2\sigma_x^s + \sin\Phi_{\mathrm{s}}^2\sigma_y^s)\tau}R_{\bar{x}}^{\mathrm{s}}, \\ \mathrm{e}^{-\mathrm{i}\tau\gamma_1(t_{\mathrm{m}})\sigma_z^{\mathrm{a}}} &= R_x^{\mathrm{a}}\mathrm{e}^{-\mathrm{i}\pi B_{\mathrm{s}}^3(\cos\Phi_{\mathrm{s}}^3\sigma_x^a + \sin\Phi_{\mathrm{s}}^2\sigma_y^a)\tau}R_{\bar{x}}^{\mathrm{a}},\end{aligned} \tag{B7}$$

where $R_{x/\bar{x}}$ denotes the $\pi/2$ or $-\pi/2$ rotation along the x direction. Under the free evolution of the NMR Hamiltonian (12), where $\nu_i^{\mathrm{RF}} = \nu_i$ ($i = 1,2$), we have

$$\mathrm{e}^{-\mathrm{i}\tau\gamma_2(t_{\mathrm{m}})\sigma_x^{\mathrm{s}}\sigma_z^{\mathrm{a}}} = R_y^{\mathrm{s}}\exp\left(-\mathrm{i}\frac{\pi J}{2}\sigma_z^{\mathrm{s}}\sigma_z^{\mathrm{a}}\tau_1\right)R_{\bar{y}}^{\mathrm{s}},$$

$$\mathrm{e}^{-\mathrm{i}\tau\gamma_3(t_\mathrm{m})\sigma_y^\mathrm{s}\sigma_z^\mathrm{a}} = R_x^\mathrm{s}\exp\left(-\mathrm{i}\frac{\pi J}{2}\sigma_z^\mathrm{s}\sigma_z^\mathrm{a}\tau_2\right)R_{\bar{x}}^\mathrm{s},$$
$$\mathrm{e}^{-\mathrm{i}\tau\gamma_4(t_\mathrm{m})\sigma_z^\mathrm{s}\sigma_z^\mathrm{a}} = \exp\left(-\mathrm{i}\frac{\pi J}{2}\sigma_z^\mathrm{s}\sigma_z^\mathrm{a}\tau_3\right), \tag{B8}$$

with the evolution times $\tau_i = 2\gamma_{i+1}(t_\mathrm{m})\tau/\pi J$ $(i = 1,2,3)$. So far, we have achieved the realization of $H_{\mathrm{s,a}}$, as shown in the pulse sequence of Fig. 2(c).

Appendix C: Experiment spectra and data

At room temperature, the thermal equilibrium state of the NMR sample is

$$\rho_\mathrm{eq} \approx \frac{1-\varepsilon}{4}I + \varepsilon\left(\frac{1}{4}I + \gamma_\mathrm{C}\sigma_z^1 + \gamma_\mathrm{H}\sigma_z^2\right), \tag{C1}$$

where $\varepsilon \approx 10^{-5}$ is the polarization, γ_C and γ_H are the gyromagnetic ratio of ^{13}C and ^{1}H nuclei. We first initialize the system to the pseudo-pure state (PPS),

$$\rho_{00}^\mathrm{PPS} \approx \frac{1-\varepsilon}{4}I + \varepsilon|00\rangle\langle 00|. \tag{C2}$$

In the experiment, the ρ_{00}^PPS was prepared from the thermal state ρ_eq using the line-selective method.[67,68] The experimental ^{13}C spectra of ρ_eq and ρ_{00}^PPS are shown in Fig. C1(a).

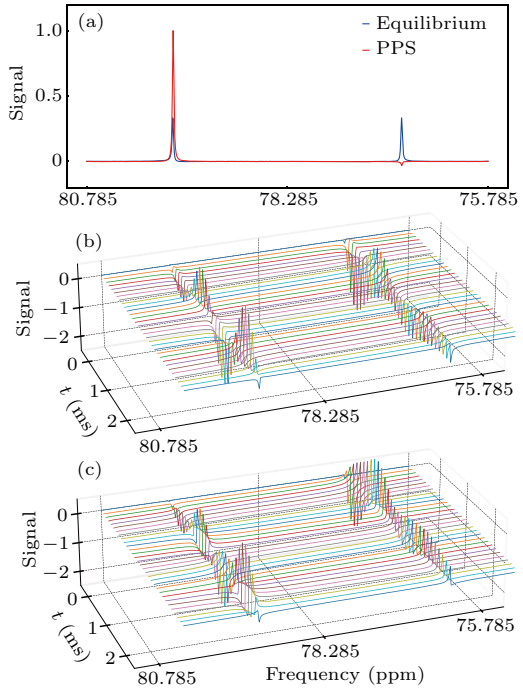


Fig. C1. (a) The experimental ^{13}C spectra of thermal equilibrium state ρ_eq (blue) and pseudo-pure state ρ_{00}^PPS (red). (b)–(c) Experimental spectra for observing the time evolutions of spin textures $\langle\psi^\mathrm{R}(k,t)|\sigma_\alpha|\psi^\mathrm{R}(k,t)\rangle$, where $\alpha = x,y$, respectively. Here $k = -0.448\pi$, and parameters are chosen as $J_0 = 1$, $J_1 = 1$ and $\delta = 0.3$.

To observe the time evolutions of spin textures $\langle\psi^\mathrm{R}(k,t)|\sigma_\alpha|\psi^\mathrm{R}(k,t)\rangle$ $(\alpha = x,y)$, we performed the measurements of $\sigma_\alpha^\mathrm{s}\otimes|0\rangle_\mathrm{a}\langle 0|$ on the dilated states (17). In the case of $k = -0.448\pi$, the corresponding spectra of $\langle\psi^\mathrm{R}(k,t)|\sigma_\alpha|\psi^\mathrm{R}(k,t)\rangle$ for different t and $\alpha = x,y$ are ploted in Figs. C1(b) and C1(c), respectively. By fitting $\langle\psi^\mathrm{R}(k,t)|\sigma_\alpha|\psi^\mathrm{R}(k,t)\rangle$, we simultaneously obtained the $\langle\varphi_\pm^\mathrm{R}|\sigma_\alpha|\varphi_\pm^\mathrm{R}\rangle$ for $\alpha = x$ or y, and also the $\phi_{yx}^{\mu\mu}(k) = \arctan[\langle\varphi_\mu^\mathrm{R}|\sigma_y|\varphi_\mu^\mathrm{R}\rangle/\langle\varphi_\mu^\mathrm{R}|\sigma_x|\varphi_\mu^\mathrm{R}\rangle]$ $(\mu = \pm)$. Figures C2(a) and C2(b) show the results of $\phi_{yx}^{\mu\mu}(k)$ for two different topological phases with $w_t = 1$ and $w_t = 2$, respectively. Thus, we got $\mathrm{Re}[\phi_{yx}(k)]$, as shown in Figs. 3(e) and 3(f).

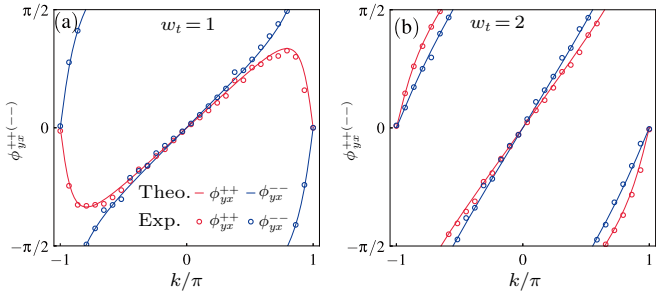


Fig. C2. The resulted $\phi_{yx}^{++}(k)$ and $\phi_{yx}^{--}(k)$ for two distinct topological phases with $w_t = 1$ and $w_t = 2$, by fitting the time evolutions of spin textures $\langle\psi^\mathrm{R}(k,t)|\sigma_\alpha|\psi^\mathrm{R}(k,t)\rangle$, where $\alpha = x,y$. The solid lines and dots are the theoretical and experimental values.

Appendix D: Error analysis

We calculated the root-mean-square $\sigma^\mathrm{Exp/Sim} = \sqrt{\Sigma_i^N(\langle\sigma_\alpha\rangle_i^\mathrm{Exp/Sim} - \langle\sigma_\alpha\rangle_i^\mathrm{Th})^2/N}$ between the measured or simulated spin textures and the theoretical values, where $\alpha = x,y$. The final state given by the simulation is $\rho_\mathrm{f}^\mathrm{sim} = U_\mathrm{Evo}G_zU_\mathrm{PPS}\rho_\mathrm{eq}U_\mathrm{PPS}^\dagger G_zU_\mathrm{Evo}^\dagger$, where G_z is a gradient magnetic field that can eliminate the off-diagonal elements of the density matrix. The spin textures come from the simulation are $\langle\sigma_\alpha\rangle = \mathrm{tr}[\rho_\mathrm{f}^\mathrm{sim}(\sigma_\alpha\otimes I + \sigma_\alpha\otimes\sigma_z)]/2$ $(\alpha = x,y)$. When considering the influence of a specific step, we simulate the 1% noise of pulses, while the rest is implemented through theoretical unitary operations. The results are listed in Table D1, where $\sigma_\mathrm{Sim}^\mathrm{Tot}$ represents the root-mean-square error of all pulses, and $\sigma_\mathrm{Read} = \sigma_\mathrm{Exp} - \sigma_\mathrm{Sim}^\mathrm{Tot}$ evaluates the readout error which came from spectral integrals. From Table D1, we find that the main errors mainly come from the preparation of the initial state, dynamical evolution, and readout.

Table D1. Results of the RMSE.

	σ_Exp	$\sigma_\mathrm{Sim}^\mathrm{Tot}$	$\sigma_\mathrm{Sim}^\mathrm{PPS}$	$\sigma_\mathrm{Sim}^\mathrm{Evol}$	σ_Read
$\langle\sigma_x\rangle$	0.0391	0.0202	0.0194	0.0197	0.0189
$\langle\sigma_y\rangle$	0.0571	0.0219	0.0079	0.0147	0.0352

Appendix E: Topological phases with and without chiral symmetry

When $h_z = 0$, the Hamilonian (1) exhibits chiral symmetry, satisfying $\sigma_z H\sigma_z = -H$. The winding number w_u $(\mu = \pm)$ can be express as

$$w_\mu = \frac{1}{2\pi}\oint_S \mathrm{d}k\frac{h_x\partial_k h_y - h_y\partial_k h_x}{(E_\mu)^2} = \frac{1}{2\pi}\oint_S \partial_k\phi_{yx}\mathrm{d}k, \tag{E1}$$

where $\phi_{yx} = \arctan(h_y/h_x)$. As an example, we consider a model with $h_x = J_0 + J_1\cos(k)$, $h_y = J_1\sin(k) - \mathrm{i}\delta$ and $h_z = 0$. Setting $J_1 = 1$, we obtain the topological phase diagram characterized by w_μ by varying δ and J_0, as shown in Fig. E1(a). The values $w_\mu = 1$, 1/2, and 0 can be obtained by integrating the gradients of $\mathrm{Re}[\phi_{yx}(k)]$ over the corresponding quasimomentum k ranges. $\mathrm{Re}[\phi_{yx}(k)]$ for different phases are shown in Figs. E1(c)–E1(e), corresponding to the three points in Fig. E1(a). In Fig. E1(b), we present the phase diagram characterized by eigenvalue winding number $\nu_\mathrm{E} = 0$ and 1, as defined in Eq. (20). Figures E1(f)–E1(h) show the energy band structures for different values of J_0, with $\delta = 0.3$. These are associated with the three marked points in Fig. E1(a). Due to the chiral symmetry of the model, the boundaries of the phase diagrams characterized by w_μ and ν_E coincide and correspond to the band-touching points ($E_\mu = 0$).

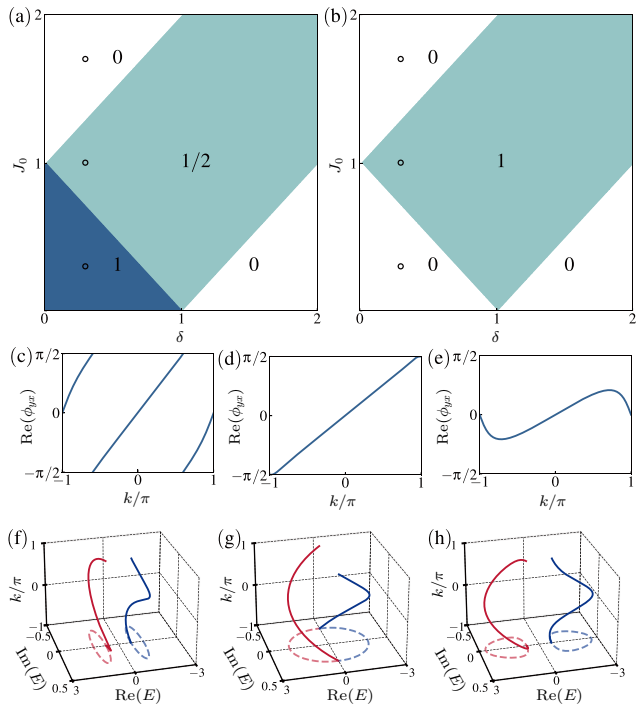


Fig. E1. (a) Phase diagram of the Hamiltonian with chiral symmetry ($h_z = 0$). The color shading from light to dark indicates $w_\mu = 0$, 1/2, and 1, as labeled. (b) Phase diagram characterized by the winding number of energy ν_E. (c)–(e) $\mathrm{Re}[\phi_{yx}(k)]$ plotted as a function of k for $\delta = 0.3$ and $J_0 = 0.3$, 1, and 1.7, respectively. (f)–(h) Energy band structures for $\delta = 0.3$ and $J_0 = 0.3$, 1, and 1.7, corresponding to $\nu_\mathrm{E} = 0$, 1, and 0, respectively.

When $h_z \neq 0$, the Hamiltonian (1) breaks the chiral symmetry. In this case, w_μ for each band is not a quantized number, showing that w_μ is no longer a topological invariant. However, their sum

$$w_t = w_+ + w_- = \frac{1}{\pi}\oint_S \partial_k \phi_{yx}\,\mathrm{d}k \tag{E2}$$

has been demonstrated to be a topological invariant.[24] We now consider the Hamiltonian (1) with $h_x = J_0 + J_1\cos(k)$, $h_y = J_1\sin(k) - \mathrm{i}\delta$ and $h_z = 0.5$, which represents a non-chiral version of the previously discussed model. Fixing $J_1 = 1$, we obtain the topological phase diagrams characterized by w_μ and ν_E by varying δ and J_0, as shown in Figs. E2(a) and E2(b), respectively. Figures E2(c)–E2(e) show the angle $\mathrm{Re}[\phi_{yx}(k)]$ for different values of J_0 and δ, as indicated in Fig. E2(a), corresponding to $w_t = 2$, 1, and 0, respectively. Figures E2(f)–E2(h) show the energy band structures corresponding to the three points in Fig. E2(b), with the associated values of $\nu_\mathrm{E} = 0$, 0, and 1, respectively. We can observe that the phase diagram in Fig. E2(a) is identical to that in Fig. E1(a), since w_t is independent of h_z. However, the phase boundaries characterized by ν_E correspond to the band-touching points and therefore change with h_z, as shown in Fig. E2(b). This means that when the Hamiltonian (1) breaks chiral symmetry, the phase diagram determined by w_t is no longer consistent with that characterized by ν_E.

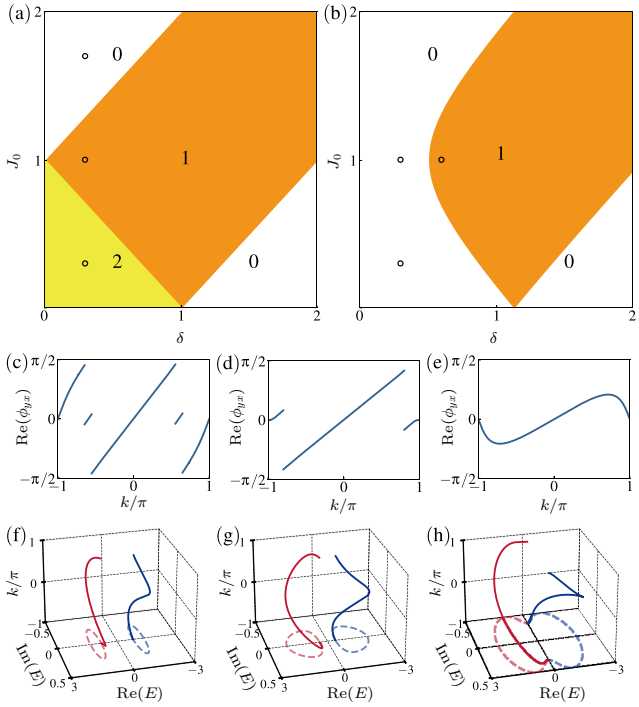


Fig. E2. (a) Phase diagram of the Hamiltonian without chiral symmetry ($h_z = 0.5$). The color shading from light to dark indicates $w_t = 0$, 1, and 2, as labeled. (b) Phase diagram characterized by the winding number of energy ν_E. (c)–(e) $\mathrm{Re}[\phi_{yx}(k)]$ plotted as a function of k for $\delta = 0.3$ and $J_0 = 0.3$, 1, and 1.7, respectively. (f)–(h) Energy band structures for different parameter values $(\delta, J_0) = (0.3, 0.3)$, (0.3, 1), and (0.6, 1), as marked in panels (b).

Acknowledgements

Project supported by the National Natural Science Foundation of China (Grant No. 11805008), Guangdong Basic and Applied Basic Research Foundation (Grant No. 2024A1515011406), the Fundamental Research Funds for the Central Universities, Sun Yat-Sen University (Grant No. 23qnpy63), and the Fund from Guangdong Provincial Key Laboratory (Grant No. 2019B121203005).

References

[1] Kitaev A Y 2003 *Annals of Physics* **303** 2

[2] Nayak C, Simon S H, Stern A, Freedman M and Das S S 2008 *Rev. Mod. Phys.* **80** 1083
[3] Hasan M Z and Kane C L 2010 *Rev. Mod. Phys.* **82** 3045
[4] Wen X G 2017 *Rev. Mod. Phys.* **89** 041004
[5] Qi X L and Zhang S C 2011 *Rev. Mod. Phys.* **83** 1507
[6] Ghatak A and Das T 2019 *J. Phys.: Condens. Matter* **31** 263001
[7] Chiu C K, Teo J C Y, Schnyder A P and Ryu S 2016 *Rev. Mod. Phys.* **88** 035005
[8] Zhou H Y and Lee J Y 2019 *Phys. Rev. B* **99** 235112
[9] Kawabata K, Shiozaki K, Ueda M and Sato M 2019 *Phys. Rev. X* **9** 041015
[10] Bergholtz E J, Budich J C and Kunst F K. 2021 *Rev. Mod. Phys.* **93** 015005
[11] Ding K, Fang C and Ma G C 2022 *Nature Reviews Physics* **4** 745
[12] Gong Z P, Ashida Y, Kawabata K, Takasan K, Higashikawa S and Ueda M 2018 *Phys. Rev. X* **8** 031079
[13] Shen H T, Zhen, B and Fu L 2018 *Phys. Rev. Lett.* **120** 146402
[14] Zhang K, Yang Z S and Fang C 2020 *Phys. Rev. Lett.* **125** 126402
[15] Yao S Y and Wang Z 2018 *Phys. Rev. Lett.* **121** 086803
[16] Yi Y F and Yang Z S 2020 *Phys. Rev. Lett.* **125** 186802
[17] Okuma N, Kawabata K, Shiozaki K and Sato M 2020 *Phys. Rev. Lett.* **124** 086801
[18] Zhang X J, Zhang T, Lu M H and Chen Y F 2022 *Adv. Phys.: X* **7** 2109431
[19] Aquino R, Lopes N and Barci D G 2023 *Phys. Rev. B* **107** 035424
[20] Rui W B, Zhao Y X and Wang Z D 2023 *Phys. Rev. B* **108** 165105
[21] Zhang L F, Tang L Z, Huang Z H, Zhang G Q, Huang W and Zhang D W 2021 *Phys. Rev. A* **103** 012419
[22] He P, Zhu Y Q, Wang J T and Zhu S L 2023 *Phys. Rev. A* **107** 012219
[23] Jiang H, Yang C and Chen S 2018 *Phys. Rev. A* **98** 052116
[24] Yin C H, Jiang H, Li L H, Lü R and Chen S 2018 *Phys. Rev. A* **97** 052115
[25] Liang S D and Huang G Y 2013 *Phys. Rev. A* **87** 012118
[26] Wojcik C C, Sun X Q, Bzdušek T and Fan S H 2020 *Phys. Rev. B* **101** 205417
[27] Hu H P and Zhao E H 2021 *Phys. Rev. Lett.* **126** 010401
[28] Lee T E 2016 *Phys. Rev. Lett.* **116** 133903
[29] Leykam D, Bliokh K Y, Huang C L, Chong Y D and Nori F 2017 *Phys. Rev. Lett.* **118** 040401
[30] Lieu S 2018 *Phys. Rev. B* **97** 045106
[31] Yao S Y, Song F and Wang Z 2018 *Phys. Rev. Lett.* **121** 136802
[32] Yokomizo K and Murakami S 2019 *Phys. Rev. Lett.* **123** 066404
[33] Kunst F K, Edvardsson E, Budich J C and Bergholtz E J 2018 *Phys. Rev. Lett.* **121** 026808
[34] Borgnia D S, Kruchkov A J and Slager R J 2020 *Phys. Rev. Lett.* **124** 056802
[35] Zhu B, Ke Y G, Zhong H H and Lee C H 2020 *Phys. Rev. Res.* **2** 023043
[36] Huang Z H, He P, Lang L J and Zhu S L 2023 *Phys. Rev. A* **107** 052205
[37] Chen L M, Zhou Y, Chen S A and Ye P 2024 *Chin. Phys. Lett.* **41** 127302
[38] Wang J J, Li F D and Yi X X 2023 *Chin. Phys. B* **32** 020305
[39] Zhang W G, Ouyang X L, Huang X Z, Wang X, Zhang H L, Yu, Y F, Chang X Y, Liu Y Q, Deng D L and Duan L M 2021 *Phys. Rev. Lett.* **127** 090501
[40] Wu Y, Wang Y H, Ye X Y, Liu W Q, Duan C K, Wang Y, Rong X and Du J F 2023 *Phys. Rev. A* **108** 052409
[41] Wang K, Dutt A, Wojcik C C and Fan S H 2021 *Nature* **598** 59
[42] Zhang Q C, Zhao L K, Liu X, Feng X L, Xiong L W, Wu W Q and Qiu C Y 2023 *Phys. Rev. Res.* **5** 023043
[43] Zeuner J M, Rechtsman M C, Plotnik Y, Lumer Y, Nolte S, Rudner M S, Segev M and Szameit A 2015 *Phys. Rev. Lett.* **115** 040402
[44] Liang C, Tang Y J, Xu A N and Liu Y C 2023 *Phys. Rev. Lett.* **130** 263601
[45] Doppler J, Mailybaev A A, Bḧm J, Kuhl U, Girschik A, Libisch F, Milburn T J, Rabl P, Moiseyev N and Rotter S 2016 *Nature* **537** 76
[46] Xiao L, Deng T S, Wang K K, Zhu G Y, Wang Z, Yi W and Xue P 2020 *Nat. Phys.* **16** 761
[47] Liu W Q, Wu Y, Duan C K, Rong X and Du J F 2021 *Phys. Rev. Lett.* **126** 170506
[48] Wang K K, Li T Y, Xiao L, Han Y W, Yi W and Xue P 2021 *Phys. Rev. Lett.* **127** 270602
[49] Cao M M, Li K, Zhao W D, Guo W X, Qi B X, Chang X Y, Zhou Z C, Xu Y and Duan L M 2023 *Phys. Rev. Lett.* **130** 163001
[50] Su R, Estrecho E, Bieganska D, Huang Y Q, Wurdack M, Pieczarka M, Truscott A G, Liew T C H, Ostrovskaya E A and Xiong Q H 2021 *Sci. Adv.* **7** eabj8905
[51] Helbig T, Hofmann T, Imhof S, Abdelghany M, Kiessling T, Molenkamp L W, Lee C H, Szameit A, Greiter M and Thomale R 2020 *Nat. Phys.* **16** 747
[52] Hu B L, Zhang Z W, Yue Z C, Liao D W, Liu Y M, Zhang H X, Cheng Y, Liu X J and Christensen J 2023 *Phys. Rev. Lett.* **131** 066601
[53] Lin Z D, Zhang L, Long X Y, Fan Y A, Li Y, Tang K, Li J, Nie X F, Xin T, Liu X J and Lu D W 2022 *npj Quantum Information* **8** 77
[54] Xu H, Mason D, Jiang L Y and Harris J G E 2016 *Nature* **537** 80
[55] Zhang H L, Jiang S, Wang X, Zhang W G, Huang X Z, Ouyang X L, Yu Y F, Liu Y Q, Deng D L and Duan L M 2022 *Nat. Commun.* **13** 4993
[56] Yu Y F, Yu L W, Zhang W G, Zhang H L, Ouyang X L, Liu Y Q, Deng D L and Duan L M 2022 *npj Quantum Information* **8** 116
[57] Ashida Y, Gong Z P and Ueda M 2020 *Adv. Phys.* **69** 249
[58] Brody D C 2013 *J. Phys. A: Math. Theor.* **47** 035305
[59] Martinez A V M, Barrios V J E and Foa T L E F 2018 *Phys. Rev. B* **97** 121401
[60] Hatsugai Y 1993 *Phys. Rev. Lett.* **71** 3697
[61] Thouless D J, Kohmoto M, Nightingale M P and den N M 1982 *Phys. Rev. Lett.* **49** 405
[62] Chang C Z, Zhang J S, Feng X, *et al.* 2013 *Science* **340** 167
[63] Asbóth J K, Oroszlány L and Pályi A 2016 *A short course on topological insulators* (Switzerland: Springer) pp. 1–44
[64] Halder D, Ganguly S and Basu S 2022 *J. Phys.: Condens. Matter* **35** 105901
[65] Wu Y, Liu W Q, Geng J P, Song X R, Ye X Y, Duan C K, Rong X and Du J F 2019 *Science* **364** 878
[66] Khaneja N, Reiss T, Kehlet C, Schulte-Herbruggen T and Glaser S J 2005 *Journal of Magnetic Resonance* **172** 296
[67] Luo Z H, Li J, Li Z K, Hung L Y, Wan Y D, Peng X H and Du J F 2018 *Nat. Phys.* **14** 160
[68] Luo Z H, Zhang W Z, Nie X F and Lu D Y 2022 arXiv: 2208.05357 [quant-ph]